The Viewing Geometry of Brown Dwarfs Influences Their Observed Colours and Variability Properties

The Astrophysical Journal, 842:78 (11pp), 2017 June 20 https://doi.org/10.3847/1538-4357/aa73cf

The Viewing Geometry of Brown Dwarfs Influences Their Observed Colors and Variability Amplitudes

Johanna M. Vos[1,2], Katelyn N. Allers[3], and Beth A. Biller[1,2]
[1] SUPA, Institute for Astronomy, University of Edinburgh, Blackford Hill View, Edinburgh EH9 3HJ, UK; jvos@roe.ac.uk
[2] Centre for Exoplanet Science, University of Edinburgh, UK
[3] Department of Physics and Astronomy, Bucknell University, Lewisburg, PA 17837, USA
Received 2017 January 19; revised 2017 April 15; accepted 2017 May 15; published 2017 June 15

Abstract

In this paper we study the full sample of known *Spitzer* [3.6 μm] and *J*-band variable brown dwarfs. We calculate the rotational velocities, $v \sin i$, of 16 variable brown dwarfs using archival Keck NIRSPEC data and compute the inclination angles of 19 variable brown dwarfs. The results obtained show that all objects in the sample with mid-IR variability detections are inclined at an angle $>20°$, while all objects in the sample displaying *J*-band variability have an inclination angle $>35°$. *J*-band variability appears to be more affected by inclination than *Spitzer* [3.6 μm] variability, and is strongly attenuated at lower inclinations. Since *J*-band observations probe deeper into the atmosphere than mid-IR observations, this effect may be due to the increased atmospheric path length of *J*-band flux at lower inclinations. We find a statistically significant correlation between the color anomaly and inclination of our sample, where field objects viewed equator-on appear redder than objects viewed at lower inclinations. Considering the full sample of known variable L, T, and Y spectral type objects in the literature, we find that the variability properties of the two bands display notably different trends that are due to both intrinsic differences between bands and the sensitivity of ground-based versus space-based searches. However, in both bands we find that variability amplitude may reach a maximum at ~7–9 hr periods. Finally, we find a strong correlation between color anomaly and variability amplitude for both the *J*-band and mid-IR variability detections, where redder objects display higher variability amplitudes.

Key words: brown dwarfs – stars: rotation – stars: variables: general – techniques: photometric

1. Introduction

Time-resolved photometric variability monitoring is a key probe of atmospheric structures in brown dwarf atmospheres, revealing a periodic modulation of the light curve as a feature rotates in and out of view. The combination of surface inhomogeneities in brown dwarf atmospheres and rapid rotation has long motivated searches for photometric variability in these objects. The first unambiguous detections (Artigau et al. 2009; Radigan et al. 2012) were high-amplitude variable objects at the L/T transition. More recently, space- and ground-based surveys in the near-IR and mid- IR have revealed that variability is common across the full range of L and T spectral types (Buenzli et al. 2014; Radigan et al. 2014; Wilson et al. 2014; Metchev et al. 2015). In fact, Metchev et al. (2015) concluded from a *Spitzer* survey that most L and T spectral type brown dwarfs display low-level variability. To date, variability has been detected in ~30 brown dwarfs, with ~5 objects displaying high-amplitude variability (>5%). Of the highest variability brown dwarfs discovered thus far, it is known that WISE 1049B is viewed roughly equator-on, with a viewing angle $i \geqslant 60°$ (Crossfield et al. 2014). For an equator-on object (with an inclination angle, $i \sim 90°$) we measure the full variability amplitude via photometric monitoring. In contrast, we measure lower variability amplitudes for low-inclination objects (Kostov & Apai 2013). In this paper, we aim to ascertain whether the range of observed amplitudes is due to properties intrinsic to each brown dwarf or whether it can be explained by consideration of their inclination angles.

A proper motion survey conducted by Kirkpatrick et al. (2010) led to the discovery of a number of L spectral brown dwarfs that were redder than the median and L-type brown dwarfs that were bluer than the median. Their kinematics revealed that they are both drawn from a relatively old population. This led to the possibility that both of these phenomena occur in the same objects, and that viewing angle determines their spectral appearance. This idea that spectral appearance is influenced by inclination angle is again suggested by Metchev et al. (2015), who find a tentative correlation between near-IR color and high-amplitude variability. If the inclination angle affects the observed amplitude as well as the observed near-IR color, then these two measurements will be related. The calculation of the inclination angle of brown dwarfs is critical in testing the relation between inclination and atmospheric appearance.

Attempts to model the cloud structure observed on variable brown dwarfs as patchy spots of thick and thin clouds have also been hindered by the unknown inclination of such objects. Walkowicz et al. (2013) performed extended numerical experiments to assess degeneracies in models of spotted light curves, and confirmed that in the absence of inclination constraints, spot latitudes cannot be determined, regardless of data quality. Apai et al. (2013) obtained high-precision *HST* near-infrared spectroscopy of the two highly variable L/T transition dwarfs 2M2139+02 and SIMP 0136. Surface brightness distributions were modeled using the inclination angle as an optimizable parameter, although the results are highly degenerate with respect to inclination, as multiple spot models with different inclinations fit the same light curve equally well. More recently, Karalidi et al. (2016) updated their *Aeolus* routine, a Markov chain Monte Carlo (MCMC) code that can map the top-of-the-atmosphere structure of an ultracool atmosphere, to fit for inclination as a free parameter and successfully retrieved an inclination of $69 \pm 8°$ for WISE 1049B, in agreement with the earlier measurement by Crossfield et al. (2014). Constraining the inclination angles of

Table 1
Variable Brown Dwarfs with Known Periods and Archival Spectra

Name	Spt	[3.6] Amp (%)	J Amp (%)	Kep Amp (%)	Period (hr)	$v \sin i$ (km s^{-1})	$(J - K_S)$	References
2M0036+18	L3.5	0.47 ± 0.05	1.22 ± 0.04	···	2.7 ± 0.3	35.12 ± 0.57	1.41	(1), (2), (3)
W0047	L6	···	10	···	13.2 ± 0.14	4.3 ± 2.2, $6.7^{+0.7}_{-1.4}$	2.55	(4), (5)
2M0103+19	L4	0.47 ± 0.05	···	···	2.7 ± 0.3	···	2.14	(1)
2M0107+00	L8	1.27 ± 0.13	···	···	5	···	2.11	(1)
SIMP 0136	T2.5	1.5 ± 0.2	5	···	2.414 ± 0.078	···	0.90	(6), (7)
SDSS0423-04	T0	···	0.8 ± 0.08	···	2 ± 0.4	···	1.54	(8)
WISE1049B*	T0.5	···	7	···	4.87 ± 0.01	26.1 ± 0.2	1.89	(9), (10), (11)
DENIS 1058*	L3	0.39 ± 0.04	0.843	···	4.3 ± 0.31	37.5 ± 2.5	1.62	(1), (12), (13)
2M1126–50	L4.5	0.21 ± 0.04	1.2 ± 0.1	···	3.2 ± 0.3	···	1.17	(1), (6)
2M1507–16	L5	0.57 ± 0.04	···	···	2.5 ± 0.1	21.27 ± 1.86	1.51	(1), (3)
2M1615+49	L4	0.9 ± 0.2	···	···	24	···	2.47	(1)
SIMP 1629	T2	···	4.3	···	>7	···	1.25	(6)
2M1721+33	L3	0.33 ± 0.07	···	···	2.6 ± 0.1	···	1.14	(1)
2M1821+14	L4.5	0.54 ± 0.05	···	···	4.2 ± 0.1	28.85 ± 0.16	1.78	(1), (3)
2M1906+40	L1	···	···	1.5	8.9	11.2 ± 2.2	1.31	(14)
PSO-318*	L7.5	···	10 ± 1	···	7.5 ± 2.5	$17.5^{+2.3}_{-2.8}$	2.78	(15), (16)
2M2139+02	T1.5	11 ± 1	26	···	7.618 ± 0.178	···	1.68	(6), (7)
2M2148+40	L6	1.33 ± 0.07	···	···	19 ± 4	···	2.38	(1)
2M2208+29	L3	0.69 ± 0.07	···	···	3.5 ± 0.2	···	1.65	(1)

Note. Starred objects are those for which we adopted $v \sin i$ values from the literature. $(J - K_S)$ colors are *2MASS*.
References. (1) Metchev et al. (2015), (2) Croll et al. (2016), (3) Blake et al. (2010), (4) Lew et al. (2016), (5) Gizis et al. (2015), (6) Radigan et al. (2014), (7) Yang et al. (2016), (8) Clarke et al. (2008), (9) Gillon et al. (2013), (10) Biller et al. (2013), (11) Crossfield et al. (2014), (12) Heinze et al. (2014), (13) Basri et al. (2000), (14) Gizis et al. (2013), (15) Biller et al. (2015), (16) Allers et al. (2016).

variable brown dwarfs will allow us to model brown dwarf atmospheres in unprecedented detail.

In this paper we study the effects of inclination angle on the observed properties of brown dwarfs for the first time. We measure the rotational velocity, $v \sin i$, of 16 variable brown dwarfs (11 of which have no previous measurement in the literature) using archival Keck data, and use estimates of radius to determine their inclination angles. We investigate the relationship between inclination angle, variability amplitude, and color anomaly. Furthermore, we investigate the entire list of known brown dwarf J-band, *Spitzer* [3.6 μm], and *Kepler* variability detections and explore the relations between variability amplitude, rotation period, and color anomaly. In Section 2 we discuss the sample of variable brown dwarfs. In Sections 3–4 we discuss the archival data and our methods in calculating inclinations. We discuss our results in Section 5.

2. The Sample

Our sample consists of all variable brown dwarfs in the L-T spectral range with published periods and high-dispersion NIRSPEC-7 data available in the Keck Archive, as well as three known variable brown dwarfs with measured periods and previously measured $v \sin i$ (WISE 1049B, DENIS 1058 and PSO-318) The full sample is shown in Table 1, and each object is described briefly below.

2MASS 0036159+182110. The object 2M0036+18 is a magnetically active L3.5 dwarf. Variability was first detected by Berger et al. (2005) in the radio, with a period of ∼3 hr. Harding et al. (2013) detected optical I-band variability, confirming the 3 hr period. 2M0036+18 was subsequently observed as part of the *Weather on Other Worlds* campaign by Metchev et al. (2015), who measured a period of 2.7 ± 0.3 hr in mid-IR wavelengths. Croll et al. (2016) measure an J-band amplitude of 1.22 ± 0.04%. Blake et al. (2010) have previously measured $v \sin i$ for this object to be 35.12 ± 0.57 km s^{-1}.

WISE J004701.06+680352.1. This very red L6 dwarf was discovered by Gizis et al. (2012). Lew et al. (2016) detect J-band variability with an amplitude of 10% and a period of ∼13 hr. They furthermore proceed to measure a $v \sin i = 6.7^{+0.7}_{-1.4}$ km s^{-1} and constrain the inclination to $i \sim 33^{+5^\circ}_{-8}$. This $v \sin i$ differs from the previously measured value of 4.3 ± 2.2 km s^{-1} by Gizis et al. (2015). Gizis et al. (2015) assign an INT-G gravity classification to W0047.

2MASS J0103320+193536. The L6 brown dwarf 2M0103+19 was first monitored by Enoch et al. (2003), who did not detect J-band variability. *Spitzer* observations later revealed mid-IR variability, with an amplitude of 0.47 ± 0.05% and a regular 2.7 hr period (Metchev et al. 2015). This object is given a β gravity classification by Faherty et al. (2012) and an INT-G classification by Allers & Liu (2013).

2MASS J01075233+0041561. The L8 object 2M0107+00 was observed as part of the *Weather on Other Worlds* campaign by Metchev et al. (2015). This is a complex and irregular variable, with an unconstrained period of 5 hr and an amplitude of 1.27 ± 0.12%.

SIMP J0136566+0933473. The variability detection of the T1.5 dwarf SIMPJ0136 by Artigau et al. (2009) was the first highly significant repeatable periodic variability of a brown dwarf at the L/T transition. Long-term monitoring of SIMPJ0136 revealed changes in both amplitude and shape over multiple rotations (Metchev et al. 2013). Yang et al. (2016) constrain the period to 2.414 ± 0.078 hr and measure a mid-IR amplitude of 1.5 ± 0.2%.

SDSS J042348.57-041403.5AB. Enoch et al. (2003) reported tentative K_S variability in this T0 binary system. Clarke et al. (2008) monitored SDSS0423-04 in the J-band and report low-level variability with a 2 hr period and a 0.8 ± 0.8%

amplitude. Radigan et al. (2014) re-observed the binary, finding inconclusive evidence for its variability during a 3.6 hr observation.

WISE J104915.57-531906.1AB. WISE 1049B (Luhman 2014) is one member of a brown dwarf binary system with spectral types L9 and T0.5 for the A and B components, respectively. Variability has been detected in both components (Biller et al. 2013; Buenzli et al. 2015a). A period of 4.87 ± 0.01 hr has been determined for the B component (Gillon et al. 2013), while a period has not been robustly observed for the A component (Buenzli et al. 2015a). Crossfield et al. (2014) report $v \sin i = 26.1 \pm 0.2$ km s^{-1}.

DENIS 1058.7-1548. Both *Spitzer* monitoring and ground-based *J*-band photometry reveal variability in this L3 dwarf (Heinze et al. 2014). DENIS 1058 has a period of 4.3 ± 0.31 hr and amplitudes of $0.39 \pm 0.04\%$ and 0.843% in the mid-IR and *J* band, respectively. This object is one of five in the sample with both a *J*-band and mid-IR variability detection. DENIS 1058 also has a published $v \sin i = 37.5 \pm 2.5$ km s^{-1} (Basri et al. 2000).

2MASS J11263991-5003550. 2M1126–50 (Folkes et al. 2007) is a peculiar L dwarf with $J - K_S$ colors that are unusually blue for its L4.5 optical or L6.5 NIR spectral type. This target was found to be variable in the *J*-band with a peak-to-peak amplitude of $1.2 \pm 0.1\%$ and a period of ~4 hr (Radigan et al. 2014; Radigan 2014). Metchev et al. (2015) later constrained the period to 3.2 ± 0.3 hr via their $0.21 \pm 0.04\%$ mid-IR variability detection.

2MASS J1507476-162738. This L5 object is another irregular variable, showing evidence of spot evolution during the 20 hr *Spitzer* observations by Metchev et al. (2015). The authors determine a period of 2.5 ± 0.1 hr and an amplitude of $0.57 \pm 0.04\%$ for this object. 2M1507–16 has previously measured $v \sin i = 21$–30 km s^{-1} (Bailer-Jones 2004; Reiners & Basri 2008; Blake et al. 2010).

2MASS J16154255+4953211. Metchev et al. (2015) detect mid-IR variability in 2M1615+49, and infer a period of 24 hr and an amplitude of $0.9 \pm 0.2\%$ from the light curve. This object is classified as VL-G by Allers & Liu (2013) based on FeH and alkali absorption as well as *H*-band shape, but it lacks the deep VO absorption observed in other low-gravity brown dwarfs. Faherty et al. (2016) assigns a γ gravity classification.

SIMP J16291841+0335380. Radigan et al. (2014) detect *J*-band variability in this T2 dwarf, with an estimated peak-to-peak amplitude of ~4.3% and a period of ~6.9 hr. These estimates are uncertain as only the trough of the light curve was caught in the 4 hr observation.

2MASS J1721039+334415. Mid-IR variability was detected in this L3 dwarf by Metchev et al. (2015), with an inferred period of 2.6 ± 0.1 hr and an amplitude of $0.33 \pm 0.07\%$.

2MASS J18212815+1414010. Metchev et al. (2015) detected mid-IR variability in this L4.5 dwarf, determining a period of 4.2 ± 0.1 hr and an amplitude of $0.54 \pm 0.05\%$. The red near-IR colors and silicate absorption (Cushing et al. 2006) of 2M1821+14 indicate an extremely dusty atmosphere, but Allers & Liu (2013) and Gagné et al. (2015) find no clear signs of low gravity. This object has a previously measured $v \sin i = 28.9$ km s^{-1} (Blake et al. 2010).

2MASS J1906485+4011068. Gizis et al. (2013) detect optical variability in this L1 dwarf using *Kepler*, finding a consistent rotation period of 8.9 hr with an amplitude of 1.5%. Gizis et al. (2013) also report $v \sin i = 11.2 \pm 2.2$ km s^{-1} and calculate the inclination, $i > 37°$. This is a magnetically active brown dwarf, so the observed variability may be due to magnetic phenomena such as starspots.

PSO 318.5–22. Biller et al. (2015) detect *J*-band variability in this extremely red exoplanet analog with amplitudes of 7%–10% during two consecutive nights of observations. PSO-318 has a period of 7.5 ± 2.5 hr (Biller et al. 2015; Allers et al. 2016). Allers et al. (2016) report a $v \sin i = 17.5^{+2.3}_{-2.8}$ km s^{-1} for this object. Liu et al. (2013) classifies this as VL-G and Faherty et al. (2016) assigns a γ classification.

2MASS J21392676+0220226. 2M2139+02 is the most variable brown dwarf discovered to date; Radigan et al. (2012) detects variability with *J*-band amplitudes of up to 26% with a period of 7.721 ± 0.005 hr. More recently, Yang et al. (2016) monitored 2M2139+02 in eight separate *Spitzer* visits, finding a period of 7.614 ± 0.178 hr, with lower mid-IR amplitudes of ~11%. 2M2139+02 is an extreme outlier, exhibiting the highest *J*-band and mid-IR variability amplitudes observed in any brown dwarf to date.

2MASS 21481628+4003593. Metchev et al. (2015) report mid-IR variability in this L6 dwarf with a period of 19 ± 4 hr and an amplitude of $1.33 \pm 0.07\%$.

2MASS 2208136+292121. Metchev et al. (2015) observed variability in this L3 brown dwarf. A period of 3.5 ± 0.2 hr and an amplitude of 0.62% were determined from the light curve. 2M2208+40 has been assigned γ and VL-G classifications (Cruz et al. 2009; Allers & Liu 2013).

2.1. Low-gravity Brown Dwarfs

As discussed in Section 2, the brown dwarfs *2M0103+19, 2M1615+49, 2M2208+29, PSO-318* and *W0047* show signs of low gravity. Low gravity is indicative of both a lower mass and a larger radius, which in turn is suggestive of a young brown dwarf that has not yet contracted to reach its equilibrium radius. This subsample provides valuable information on the effects of gravity and youth on variability properties. Metchev et al. (2015) note a tentative correlation between low-gravity and high-amplitude mid-IR variability amplitudes. This correlation is further supported by a number of high-amplitude *J*-band detections in low-gravity objects (Biller et al. 2015; Lew et al. 2016). This is unexpected because atmospheric models typically require very thick clouds (Madhusudhan et al. 2011), and initial variability studies suggest that objects with patchy clouds in the process of breaking up tend to have the highest variability amplitudes (Radigan et al. 2014). Evidently, low-gravity objects can exhibit very different atmospheric properties to field brown dwarfs, and they are denoted by a black inset in all plots in this paper.

3. Data and Observations

We obtained high-dispersion NIRSPEC spectra for our targets from the Keck Observatory Archive. NIRSPEC is a near-infrared echelle spectrograph on the Keck II 10 m telescope on Maunakea, Hawaii. The NIRSPEC detector is a 1024×1024 pixel ALADDIN InSb array. Observations were carried out using the NIRSPEC-7 (1.839–2.630 μm) passband in echelle mode using the 3-pixel slit (0.″432), an echelle angle of 62.°67–63.°00, and a grating angle of 35.°46–35.°52. Observations of targets were gathered in nod pairs, allowing for the removal of sky emission lines through the subtraction of two consecutive images. Arclamps were observed for

Table 2
NIRPSEC-7 High Dispersion Observing Information

Name	UT Date	Slit Name	Echelle (deg)	Cross Disp (deg)	Exp Time (s)	Airmass	S/N	Prog ID
2M0036+18	2011 Sep 10	0.432 × 12	63.00	35.52	2 × 450	1.006	28	U049NS
W0047	2013 Sep 17	0.432 × 12	62.97	35.51	2 × 1200	1.507	24	U055NS
2M0103+19	2014 Jul 19	0.432 × 24	62.68	35.44	2 × 300	1.209	10	N160NS
2M0107+00	2011 Sep 07	0.432 × 12	63.00	35.46	2 × 1500	1.070	24	U049NS
SIMP1036	2011 Sep 10	0.432 × 12	63.00	35.52	2 × 600	1.061	17	U049NS
SDSS0423-04	2004 Mar 08	0.432 × 12	62.65	35.51	2 × 1200	1.342	21	C13NS
2M1126–50	2014 Jan 20	0.432 × 12	63.02	35.53	2 × 600	2.892	15	U055NS
2M1507–16	2011 Jun 10	0.432 × 12	63.00	35.53	2 × 600	1.288	19	U038NS
2M1615+49	2011 Sep 10	0.432 × 12	63.00	35.52	2 × 900	1.491	21	U049NS
SIMP 1629	2011 Sep 07	0.432 × 12	63.00	35.46	2 × 1200	1.119	24	U049NS
2M1721+33	2011 Sep 07	0.432 × 12	63.00	35.46	2 × 1000	1.254	27	U049NS
2M1821+14	2006 Jul 30	0.432 × 12	62.67	35.51	2 × 600	1.075	26	N050NS
2M1906+40	2011 Sep 10	0.432 × 12	63.00	35.52	2 × 120	1.631	10	U049NS
2M2139+02	2011 Sep 07	0.432 × 12	63.00	35.46	2 × 1200	1.048	23	U049NS
2M2148+40	2006 Dec 32	0.432 × 12	62.68	35.52	2 × 750	1.451	22	N044NS
2M2208+29	2011 Sep 10	0.432 × 12	63.00	35.52	2 × 1500	1.054	27	U049NS

Note. All data were taken from the Keck archive.

wavelength calibration. 5–10 flat field and dark images were taken for each target to account for variations in sensitivity and dark current on the detector. Details of the observations are given in Table 2.

4. Data Reduction Methods

Data were reduced using a modified version of the REDSPEC reduction package to spatially and spectrally rectify each exposure. The KECK/Nirspec Echelle Arc Lamp Tool was used to identify the wavelengths of lines in our arc lamp spectrum. We focus our analysis on order 33 since this part of the spectrum contains a good blend of sky lines and brown dwarf lines, allowing for an accurate fit. Order 33 is also commonly used in the literature for NIRSPEC high-dispersion N-7 spectra (Blake et al. 2010; Gizis et al. 2013). We additionally reduced orders 32 and 38, which again contain a sufficient amount of sky and brown dwarf lines, to check for consistency. After nod-subtracting pairs of exposures, we created a spatial profile that is the median intensity across all wavelengths at each position along the slit. To remove any residual sky emission lines from our nod-subtracted pairs, we identified pixels in the spatial profile that did not contain significant source flux. We used Poisson statistics to determine the noise per pixel at each wavelength. We extracted the flux within an aperture in each nod-subtracted image to produce two spectra of our source. The extracted spectra were combined using a robust weighted mean with the xcombspec procedure from the SpeXtool package (Cushing et al. 2004).

4.1. Determining Rotational Velocities

We used the approach outlined in Allers et al. (2016) to determine the rotational velocities of our objects. We employed forward modeling to simultaneously fit the wavelength solution of our spectrum, the rotational and radial velocities, the scaling of telluric line depths, and the FWHM of the instrumental line spread function (LSF). We used the BT-Settl model atmospheres (Allard et al. 2012) as the intrinsic spectrum for each of our objects. Further details can be found in Allers et al. (2016). In total, the forward model has nine free parameters: the $T_{\rm eff}$ and $\log(g)$ of the atmosphere model, the v_r and $v \sin i$ of the brown dwarf, τ for the telluric spectrum, the LSF FWHM, and the wavelengths of the first, middle, and last pixels. The forward model was compared to our observed spectrum, and the parameters used to create the forward model were adjusted to achieve the best fit.

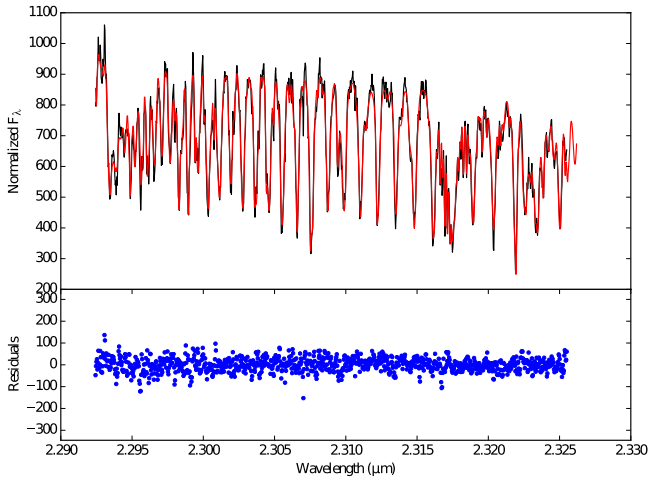

Figure 1. Observed spectrum of 2M1507–16 (black) compared to our forward model with best-fit parameters (red).

To determine the best-fit parameters of our forward model as well as their marginalized distributions, we used an MCMC approach. This involves creating forward models that allow for a continuous distribution of $T_{\rm eff}$ and $\log(g)$ by linearly interpolating between atmosphere grid models. We employed the DREAM (ZS) algorithm (ter Braak & Vrugt 2008), which uses an adaptive stepper, updating model parameters based on chain histories. An example of our best-fit model for 2M1507–16 order 33 is shown in Figure 1. Table 3 shows the resulting rotational velocities, radial velocities, effective temperatures, and surface gravities calculated using order 33. We also find that orders 32 and 38 are consistent with the results obtained from order 33.

As discussed in Section 2, five of the objects in our sample have previous measurements of $v \sin i$. Our value of $35.91^{+0.8}_{-0.8}$ km s^{-1}

Table 3
Rotational Velocities, Radial Velocities, Effective Temperatures, and Gravities Calculated in this Study

Name	$v \sin i$ (km s^{-1})	RV (km s^{-1})	$T_{\rm eff}$ K	$\log(g)$ dex	Radius ($R_{\rm Jup}$)	Inclination (°)
2M0036+18	36.0 ± 0.2	20.9 ± 0.14	1909 ± 6	5.22 ± 0.02	0.94–1.08[a]	51 ± 9
W0047	9.8 ± 0.3	$-19.8^{+0.1}_{-0.2}$	1666 ± 2	$5.16^{+0.2}_{-0.3}$	1.26–1.34[a]	53 ± 3
2M0103+19	$40.0^{+3.7}_{-4.7}$	$12.4^{+3.8}_{-4.0}$	1880^{+200}_{-110}	$4.0^{+0.6}_{-0.4}$	1.21–1.47[a]	40 ± 8
2M0107+00	19.4 ± 0.8	8.2 ± 0.5	1450^{+70}_{-20}	$4.7^{+0.4}_{-0.1}$	0.87–1.09[a]	56 ± 17
SIMP 0136	$52.8^{+1.1}_{-1.0}$	12.3 ± 0.8	1290 ± 10	$5.45^{+0.03}_{-0.04}$	0.8–1.2	80 ± 12
SDSS 0423-04	68.0 ± 0.9	30.5 ± 0.6	1460 ± 10	$5.27^{+0.5}_{-0.04}$	0.8–1.2	79^{+11}_{-16}
WISE 1049B[b]	26.1 ± 0.2	…	…	…	0.95–1.09[a]	83^{+7}_{-8}
DENIS 1058[c]	37.5 ± 2.5	…	…	…	0.93–1.07[a]	90_{-2}
2M1126–50	$22.8^{+1.6}_{-2.4}$	49.3 ± 1.1	1270^{+60}_{-20}	$3.7^{+0.5}_{-0.1}$	0.8–1.2	35 ± 7
2M1507–16	19.1 ± 0.5	$-39.2^{+0.3}_{-0.4}$	1750 ± 6	5.45 ± 0.04	0.9–1.08[a]	23 ± 2
2M1615+49	$9.5^{+1.3}_{-1.2}$	-21.3 ± 0.5	1624^{+8}_{-48}	$4.53^{+0.08}_{-0.1}$	1.1–1.4	86^{+4}_{-10}
SIMP 1629	$19.7^{+0.7}_{-0.8}$	7.7 ± 0.5	1277 ± 7	5.29 ± 0.03	0.8–1.2	82^{+8}_{-13}
2M1721+33	21.5 ± 0.3	-102.8 ± 0.2	1656 ± 2	4.77 ± 0.02	0.8–1.2	27 ± 4
2M1821+14	30.7 ± 0.2	11.0 ± 0.1	1766 ± 1	4.89 ± 0.01	0.8–1.2	61 ± 17
2M1906+40	15.2 ± 0.5	$-22.8^{+0.3}_{-0.2}$	1999^{+3}_{-5}	5.30 ± 0.04	0.8–1.2	82^{+8}_{-12}
PSO-318[d]	$17.5^{+2.3}_{-2.8}$	$6.0^{+0.8}_{-1.1}$	1325^{+330}_{-12}	$3.7^{+1.1}_{0.1}$	1.38–1.44[a]	61 ± 17
2M2139+02	18.7 ± 0.3	-25.1 ± 0.3	1333 ± 5	5.37 ± 0.02	0.8–1.12[a]	90_{-1}
2M2148+40	$9.2^{+0.4}_{-0.3}$	-14.3 ± 0.1	1774 ± 1	$5.00^{0.01}_{-0.02}$	0.89–1.09[a]	88^{+2}_{-8}
2M2208+29	$40.6^{+1.3}_{-1.4}$	$-15.7^{+0.8}_{-0.9}$	1707^{+10}_{-9}	4.27 ± 0.11	1.21–1.61[a]	55 ± 10

Notes. The results presented here are for order 33. The last two columns show our estimated radii and the resulting angle of inclination calculated for each object.
[a] Radii are taken from Filippazzo et al. (2015).
[b] $v \sin i$ measurement taken from Crossfield et al. (2014).
[c] $v \sin i$ measurement taken from Basri et al. (2000).
[d] Measurements taken from Allers et al. (2016).

for 2M0036+18 is consistent with the $v \sin i$ measured by Blake et al. (2010). Literature $v \sin i$ measurements for 2M1507–16 have ranged from 21–30 km s^{-1} (Bailer-Jones 2004; Reiners & Basri 2008; Blake et al. 2010), and we find that our measurement of $19.21^{+0.53}_{-0.53}$ km s^{-1} is consistent with the Blake et al. (2010) measurement. Our measurement of $30.61^{+0.69}_{-0.69}$ km s^{-1} for 2M1821+14 is slightly larger than the Blake et al. (2010) measurement of 28.9 ± 0.16 km s^{-1}, but is in agreement within 2σ. Our $v \sin i$ measurement for 2M1906+40 is slightly larger than the Gizis et al. (2013) measurement, but is again consistent within 2σ. Finally, our measurement of $9.6^{+0.49}_{-0.49}$ km s^{-1} for W0047 is higher than both previous measurements by Gizis et al. (2015) and Lew et al. (2016). The model atmosphere for W0047 used by Gizis et al. (2015) has $T_{\rm eff} = 2300$ and $\log(g) = 5.5$, while evolutionary models predict $T_{\rm eff} = 1270$ and $\log(g) = 4.5$ (Gizis et al. 2015). Our model (with $T_{\rm eff} = 1670$ and $\log(g) = 5.2$) is in better agreement with the evolutionary model results. With higher effective temperature and surface gravity, the atmospheric model used by Gizis et al. (2015) will include more pressure broadening, and thus result in a lower value of $v \sin i$. Lew et al. (2016) do not provide details on the atmospheric model used. Again, the consistency between orders 32, 33, and 38 further supports our results.

4.2. Calculating Inclination Angles

We assumed that the brown dwarf rotates as a rigid sphere. However, this is not strictly true. The rotational period of Jupiter, as measured by magnetic fields originating in the core, is $9^{\rm h}50^{\rm m}30^{\rm s}$, whereas the period measured using features rotating along the equator is $9^{\rm h}55^{\rm m}40^{3}$, a difference of only 5 minutes. Since rotational periods as measured from photometric variability in general have much larger uncertainties, the rigid-body assumption is reasonable for our analysis. Thus, the equatorial rotation velocity, v, is given by $v = 2\pi R/P$, where R is the radius of the brown dwarf and P is its rotation period. With our measured values of $v \sin i$ in hand, an assumption of radius and a measurement of the rotation period allow us to determine the angle of inclination, i. Filippazzo et al. (2015) provide radius estimates from evolutionary models for 11 of 19 of our targets (starred in Table 3). We use reasonable radius estimates for the remaining field brown dwarfs. At field brown dwarf ages, the radii are independent of mass because of the electron degeneracy (Burrows et al. 2001) and approach the radius of Jupiter. Therefore, the field brown dwarf targets are assumed to have a radius of 0.8–1.2 $R_{\rm Jup}$. 2M1615+49 is the only young brown dwarf with no radius estimate. Since it has not been associated with any moving group (Faherty et al. 2016), we have no age constraint on this object. We assume a radius of 1.1–1.7 $R_{\rm Jup}$, similar to other VL-G objects in the sample. A Monte Carlo analysis was used to determine the inclination, i for each target, using uniformly distributed radii and Gaussian distributions for the $v \sin i$ and period values. When values for sin(i) fell above 1, we set these values to 1, as discarding them would bias our results towards lower inclinations. These values likely arise due to an overestimated period or an underestimated radius. While these values are unphysical, they suggest a larger inclination angle. Discarding the unphysical values in the Monte Carlo analysis, as done by Gagné et al. (2017), results in lower inclinations for some objects, but does not effect the overall results. The inclination and error were calculated as the mean and standard deviation of the resulting distribution of i. Table 3

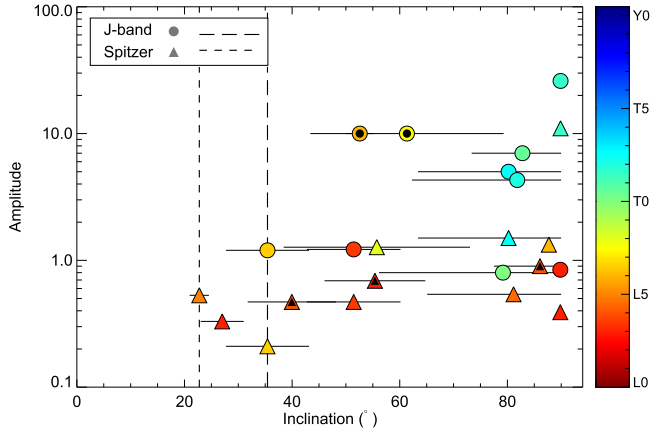

Figure 2. Variability amplitude plotted against inclination angle for our sample. Circles denote *J*-band detections, while triangles denote *Spitzer* 3.6 μm detections. The color scale represents the spectral type, and young objects are denoted by a black inset. Dashed lines represent the minimum inclination angle for each band.

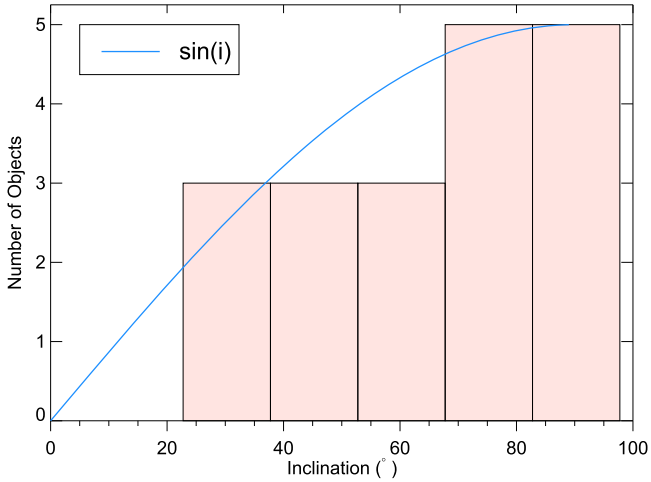

Figure 3. Histogram showing the distribution of inclinations in our sample. The probability distribution of randomly oriented objects is $P(i) \sim \sin(i)$. This distribution fits the calculated distribution quite well.

shows the rotational velocities calculated for our sample, as well as the inclination angles determined based on our estimated radii. As stated earlier, we focus our analysis on order 33. However, using a weighted average of $v \sin i$ values obtained from orders 32, 33, and 38 yields consistent inclination angles.

5. Results and Discussion

5.1. Effects of Inclination on Variability Amplitude

Figure 2 shows the variability amplitude plotted against the angle of inclination. We note a number of interesting trends in the *J*-band and *Spitzer* variable brown dwarfs.

First, the highest amplitude *J*-band variable objects are either L/T transition brown dwarfs or young, red brown dwarfs. The highest *Spitzer* and *J*-band amplitudes are both for the L/T transition brown dwarf, 2M2139+02. The *Spitzer* amplitudes for young brown dwarfs are slightly enhanced, but only relative to their own spectral type and not the entire *Spitzer* sample.

Second, while it is clear that each brown dwarf has its own intrinsic amplitude, the inclination angle affects the observed amplitude for both bands. Figure 2 shows that there are no mid-IR variability detections at inclination angles $<20°$ and no *J*-band detections at inclination angles $<35°$. For a sample of objects with random orientation, the probability distribution of the inclination angles is $P(i) \sim \sin i$ (Jackson & Jeffries 2010). Thus, the overall observed distribution is fairly consistent with the distribution expected for brown dwarfs that are randomly oriented in space (Figure 3). This means that although our sample is small, it is representative of the brown dwarf population with regard to inclination. Excluding the young objects, we find relatively low amplitudes at inclination angles 20°–60°. At inclinations close to 90°, we observe the highest variability amplitudes in both bands. This makes sense as the brown dwarf is nearly equator-on, allowing us to observe the full variability amplitude. An atmospheric feature observed on a low-inclination object will appear smaller as a result of projection effects.

The *J*-band amplitudes appear to be more affected by inclination than the *Spitzer* amplitudes. The highest *J*-band variable objects appear at high inclinations, whereas a *Spitzer* brown dwarf viewed equator-on displays similar amplitudes to those observed at inclinations as low as $\sim 20°$. This may be explained by considering the pressures probed by each band. Biller et al. (2013), Buenzli et al. (2012), and Yang et al. (2016) determined the pressure level probed at optical depth $\tau = 2/3$ as a function of wavelength for various models, finding that the *J*-band probes a discrete range of pressures deep in the atmosphere. On the other hand, the *Spitzer* [3.6 μm] band probes a broader range of pressures that extends higher up in the photosphere. For the deep layers probed by the *J*-band, the flux will be strongly attenuated for the low-inclination objects because of an increased path length through the atmosphere. The effect is not observed as strongly for *Spitzer* detections because more of the flux originates from near the top of the photosphere. Thus, we see *J*-band amplitudes decrease strongly with decreasing inclination.

We used a toy model to investigate the effects of inclination on the observed variability amplitude. Our model has two terms:

$$A = A_0 \sin i - \kappa \frac{dx}{\sin i}, \quad (1)$$

where A is the observed amplitude and A_0 is the amplitude that would be observed if there were no atmospheric attenuation of the flux. κ is the factor by which the flux is attenuated as it passes through the atmosphere, and $\frac{dx}{\sin i}$ is the atmospheric path length. The first term is a projection effect that causes the observed area of a spot to decrease as the brown dwarf approaches lower inclinations. The second term represents the attenuation of the flux as it passes through the brown dwarf atmosphere. Figure 4 shows that decreasing the inclination angle increases the atmospheric path length. From the models discussed above, we expect that the *J*-band path lengths are larger than the *Spitzer* path lengths. We fit the function for both bands, assuming that all objects have the same intrinsic amplitude. We considered only the field brown dwarfs since young objects will have very different atmospheric structures. The best-fit parameters are shown in Table 6, with the functions plotted in Figure 5. The model fits the data reasonably well, displaying the earlier drop-off of the *J*-band amplitudes compared to the *Spitzer* amplitudes that is due to a much larger *J*-band $\kappa dx/\sin i$ term. We estimate the brown dwarf atmospheric extinction as a power law: $\kappa \sim \lambda^{-\alpha}$, where $\alpha = 1.7$

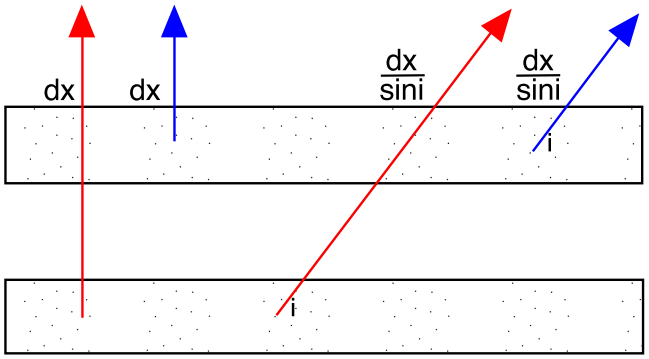

Figure 4. Inclination angle i affects the atmospheric path length traveled from flux originating from a certain depth. In this diagram, the bottom shaded area corresponds to the depth that most of the J-band flux originates from when an object is viewed equator-on. The top shaded area corresponds to the depth that most of the *Spitzer* 3.6/*mu*m flux comes from for an equator-on object. At $i = 90°$, the flux is attenuated by κdx where κ is the attenuation coefficient and dx is the distance to the top of the atmosphere. At $i < 90°$ this flux is more strongly attenuated because the atmospheric path length is longer.

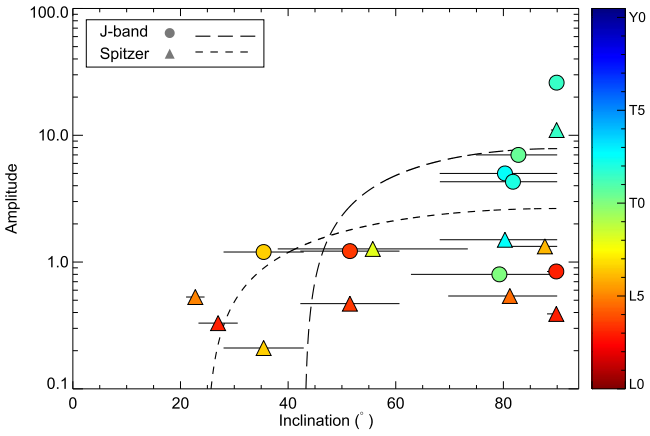

Figure 5. Variability amplitude plotted against inclination angle for *Spitzer* 3.6 μm (triangles) and J-band (circles) field objects in our sample. The color scale represents the spectral type, and young objects are denoted by a black inset. Best-fit functions of Equation (1) are plotted as gray dashed lines.

(Bertoldi et al. 1999). While this is an empirical law based on extinction by the interstellar medium, dust grains found in the atmospheres of brown dwarfs may be similar in size and thus produce similar results (Looper et al. 2010; Marocco et al. 2014). Thus, by estimating the extinction coefficient, we can estimate the relative path lengths traveled by the flux in each band. We find that $dx_{3.6\mu m}/dx_J = 0.40$. Yang et al. (2016) calculate the pressure levels probed at optical depth $\tau = 2/3$ as a function of wavelength for models with a range of spectral types. For all spectral types investigated, they find that the J-band probes a discrete range of pressures deep in the atmosphere, while the pressures probed by the *Spitzer* [3.6 μm] extend higher in the atmosphere. The relative pressures found in this study for L5, T2, and T6 brown dwarfs were $P_{3.6\mu m}/P_J = 0.39$, 0.05 and 0.05, respectively. If we assume that the depth increases monotonically with pressure, then our value of $dx_{3.6\mu m}/dx_J$ is consistent with that of the L5 brown dwarf computed by Yang et al. (2016). Of course this is a highly simplistic model with some limitations. First, it does not take into account spectral types or different intrinsic variabilities. Second, since the majority of J-band variability

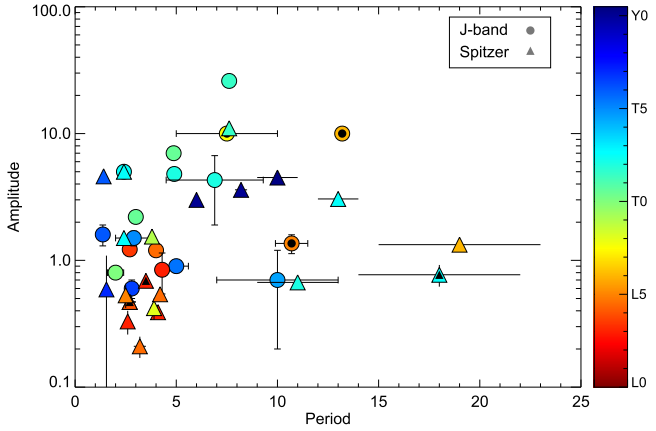

Figure 6. Variability amplitude plotted against period for *Spitzer* 3.6 μm (triangles) and J-band (circles) variability detections. The color bar represents the spectral type of each object, and young objects are denoted by a black inset. Objects with unconstrained periods from were not included. Data and literature references are shown in Tables 2 and 3.

detections are made from ground-based surveys, they are not sensitive to the lower amplitudes detected by *Spitzer* in the mid-IR. Third, the model fits are strongly influenced by the absence of detections at low amplitudes, but the reason may be the underlying inclination distribution and not that their variability amplitudes are below detection limits.

5.2. Relation between Period and Variability Amplitude

Figure 6 shows the variability amplitude plotted against rotation period for *Spitzer* and J-band variable L, T, and Y spectral type objects with published periods from the literature (shown in Tables 2 and 3). The mid-IR *Spitzer* detections are extremely robust because of the high photometric precision that is achievable from space. Additionally, these observations are typically longer than ground-based observations—for example, Metchev et al. (2015) employ ~20 hr observations in their survey. This results in extremely accurate period measurements for *Spitzer*-monitored objects. In contrast, the J-band detections come from a variety of ground-based and space-based *HST* surveys. The ground-based searches do not reach the same photometric precision as space-based searches and thus are limited to higher amplitudes. J-band monitoring observations are shorter than *Spitzer* observations and thus have larger period uncertainties. For both samples, we only take objects whose periods are constrained.

The J-band and *Spitzer* data display notably different period and variability amplitude properties. Ground-based J-band detections have lower photometric precision, so in general J-band detections are limited to larger amplitudes. It is clear that mid-IR variability is intrinsically lower than near-IR variability, but as high-amplitude variability would certainly have been detected with *Spitzer*. Ground-based observations are only sensitive to shorter periods (>15 hr), so the longer period variable brown dwarfs have been detected with *Spitzer*.

Figure 7 shows the variability amplitude plotted against rotation period for all J-band variable objects with published periods (shown in Table 4). Measured periods are <15 hr, since most J-band detections are ground-based, and thus are sensitive to this range of periods. The highest amplitudes are L/T transition spectral types, as reported by Radigan et al. (2014). The young, low-gravity L-type objects W0047, PSO-318, and

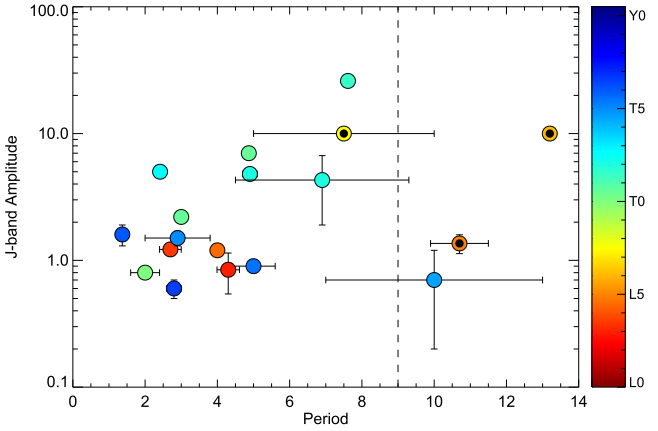

Figure 7. Variability amplitude plotted against period for J-band variability detections. The color bar shows the spectral type, and young objects are denoted by a black inset. The dashed line shows the cut-off point of the period range for which the Rhines scale appears to have an effect on variability amplitude. For rotation periods <9 hr, we find a tentative correlation between variability amplitude and period with a p-value = 6.7%.

Table 4
Rotational Periods and Peak-to-peak Variability Amplitudes for J-band Variable Brown Dwarfs

Name	Spt	Period (hr)	J-band Amp (%)	References
2M0036+18	L3.5	2.7 ± 0.3	1.22 ± 0.04	(1)
W0047	L6	13.2 ± 0.14	10 ± 0.5	(2)
SIMP 0136	T2.5	2.414 ± 0.078	5	(3), (4)
SDSS 0423-04	T0	2 ± 0.4	0.8 ± 0.08	(5)
2M0559	T4.5	10 ± 3	0.7 ± 0.5	(3)
SDSS 0758	T2	4.9 ± 0.2	4.8 ± 0.2	(3)
2M0817	T6.5	2.8 ± 0.2	0.6 ± 0.1	(3)
WISE 1049B	T0.5	4.87 ± 0.01	7 ± 0.5	(6), (7)
SDSS 1052	T0.5	3 ± 0.5	2.2 ± 0.5	(8)
DENIS 1058	L3	4.3 ± 0.31	0.843 ± 0.098	(9)
2M1126–50	L4.5	3.2 ± 0.3	1.2 ± 0.1	(3)
2M1207b	L5	10.7 ± 0.8	1.36 ± 0.23	(10)
SIMP 1629	T2	6.9 ± 2.4	4.3 ± 2.4	(3)
2M1828	T5.5	5.0 ± 0.6	0.9 ± 0.1	(3)
PSO-318	L7.5	7.5 ± 2.5	10 ± 1	(11), (12)
2M2139+02	T1.5	7.614 ± 0.178	26	(4), (13)
2M2228	T6	1.369 ± 0.032	1.6 ± 0.3	(3), (4)
2M2331	T5	2.9 ± 0.9	1.5 ± 0.2	(5)

References. (1) Croll et al. (2016), (2) Lew et al. (2016), (3) Radigan et al. (2014), (4) Yang et al. (2016), (5) Clarke et al. (2008), (6) Gillon et al. (2013), (7) Biller et al. (2013), (8) Girardin et al. (2013), (9) Heinze et al. (2014), (10) Zhou et al. (2016), (11) Biller et al. (2015), (12) Allers et al. (2016), (13) Radigan et al. (2012).

HNPegb display higher variability amplitudes than other L dwarfs, supporting a tentative correlation between low-gravity and high-amplitude variability reported by Metchev et al. (2015). Additionally, for periods ∼7–9 hr, there seems to be an overall increase in J-band variability amplitude with longer periods. We calculated the significance of this result by calculating Kendall's τ using IDLs *r_correlate.pro*. Kendall's τ is a nonparametric measure of correlation based on the relative ordering of the rank of each value in the data set (Press et al. 1987). To define τ, we started with N data points (x_i, y_i) and considered all $\frac{1}{2}N(N-1)$ pairs of data points. A pair is *concordant* if the relative ordering of the ranks of (x_i, x_j) is the same as the relative ordering of the ranks of (y_i, y_j). A pair is *discordant* if the relative ordering of (x_i, x_j) differs from the ordering of the (y_i, y_j) ranks. When the relative (x_i, x_j) ranks are the same, we call the pair an "extra-y" pair. Similarly, when relative (x_i, x_j) ranks are the same, we get an "extra-x" pair. Kendall's τ is then calculated using the equation

$$\tau = \frac{C - D}{\sqrt{C + D + \text{extra} - y}\sqrt{C + D + \text{extra} - x}}, \quad (2)$$

where C and D are the number of concordant and discordant pairs, respectively. In the null hypothesis of no association between x and y, τ is normally distributed with zero-expectation value and a variance of

$$\text{Var}(\tau) = \frac{N + 10}{9N(N-1)}. \quad (3)$$

Using this distribution, we calculated the probability of obtaining a value $\geqslant t$ assuming that no correlation exists. This is known as the p-value.

Calculating the Kendall's τ rank correlation coefficient and p-value, we find that the relation between J-band variability amplitude and rotational period (for periods <9 hr) is significant with a p-value = 6.7%. In contrast, including all periods, the correlation between period and amplitude is not significant, with a p-value = 17%. This tentative correlation between variability amplitude and rotation period for periods <9 hr may be explained by consideration of the Rhines length (Rhines 1970). Organized jet features in the atmospheres of the giant solar system planets generally scale in size with the Rhines length. This also represents the maximum attainable size that a coherent atmospheric structure can grow to before being destroyed by such zonal jets. The Rhines length is given by

$$L_{\text{RH}} \sim \sqrt{\frac{U}{2\Omega R \cos\phi}}, \quad (4)$$

where U is the characteristic wind speed, R is the radius, $\Omega = 2\pi/P$, where P is the period, and ϕ is the latitude of the atmospheric feature. When the wind speeds and latitudes are the same, then $L_{\text{RH}} \sim \sqrt{P}$. Thus we would expect the maximum atmospheric feature size to increase with longer rotational periods, explaining the increasing variability amplitude with period in Figure 7. Beyond periods of 9 hr, this correlation does not seem to hold. This suggests that for periods greater than ∼7–9 hr, the Rhines length is no longer the dominant factor in controlling the size of atmospheric features.

Figure 8 shows the *Spitzer* amplitudes plotted against rotation periods for all *Spitzer* variable objects with published periods (presented in Table 5). *Spitzer* observations are in general longer than ground-based J-band observations (Metchev et al. (2015) employed ∼20 hr observations for their *Spitzer* survey) and are thus sensitive to longer periods. *Spitzer* light curves have much higher photometric precision than ground-based studies and thus are also sensitive to lower amplitudes. However, the mid-IR variability is clearly intrinsically lower than the near-IR variability. In contrast to the J-band data, Kendall's τ produces p-value ∼80%, thus we find no correlation between variability amplitude and rotation period in this case. At longer periods, the observed variability amplitudes appear to decrease, but the sparse number of data points prevents us from confirming this. The highest variability

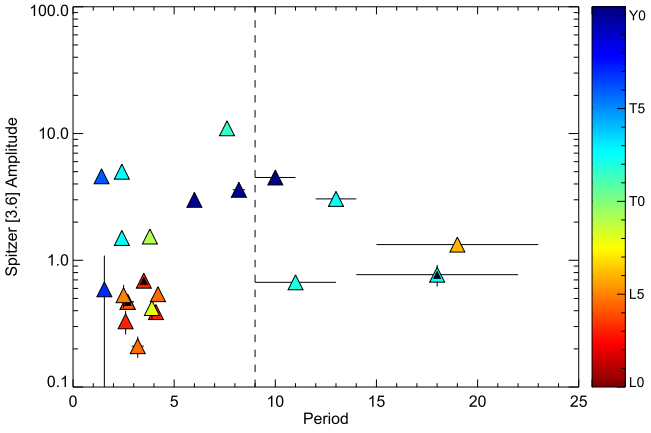

Figure 8. Same as Figure 7, but showing *Spitzer* variability detections.

Table 5
Rotational Periods and Peak-to-peak Variability Amplitudes for *Spitzer* [3.6]μm Variable Brown Dwarfs

Name	Spt	Period (hr)	[3.6] μm Amp (%)	References
2M0036+18	L3.5	2.7 ± 0.3	0.47 ± 0.05	(1)
2M0050	T7	1.55 ± 0.02	<0.59 ± 0.50	(1)
2M0103+19	L6	2.7 ± 0.1	0.56 ± 0.03	(1)
2M0107+00	L8	5 ± 10	1.27 ± 0.13	(1)
SIMP 0136	T2.5	2.414 ± 0.078	1.5 ± 0.2	(2)
2M0825	L7.5	7.6 ± 10	0.81 ± 0.08	(1)
WISE0855	Y1	10 ± 1	4.5 ± 0.5	(3)
SDSS1043	L9	3.8 ± 0.2	1.54 ± 0.15	(1)
DENIS 1058	L3	4.1 ± 0.2	0.39 ± 0.04	(1)
2M1126–50	L4.5	3.2 ± 0.3	0.21 ± 0.04	(1)
2M1324	T2.5	13 ± 1	3.05 ± 0.15	(1)
WISE1405	Y0.5	8.2 ± 0.3	3.6 ± 0.4	(4)
2M1507–16	L5	2.5 ± 0.1	0.53 ± 0.11	(1)
SDSS1511	T2	11 ± 2	0.67 ± 0.07	(1)
SDSS1516	T0.5	6.7 ± 10	2.4 ± 0.2	(1)
2M1615+49	L4	24 ± 10	0.9 ± 0.2	(1)
2M1632	L8	3.9 ± 0.2	0.42 ± 0.08	(1)
2M1721+33	L3	2.6 ± 0.1	0.33 ± 0.07	(1)
WISE1738	Y0	6.0 ± 0.1	3 ± 0.1	(5)
2M1753	L4	50 ± 10	0.25 ± 0.5	(1)
2M1821+14	L4.5	4.2 ± 0.1	0.54 ± 0.05	(1)
HNPegB	T2.5	18 ± 4	0.77 ± 0.15	(1)
2M2148+40	L6	19 ± 4	1.33 ± 0.07	(1)
2M2139+02	T1.5	7.618 ± 0.18	11 ± 1	(2)
2M2208+29	L3	3.5 ± 0.3	0.69 ± 0.07	(1), (2)
2M2228	T6	1.37 ± 0.01	4.6 ± 0.2	(1)

References. (1) Metchev et al. (2015), (2) Yang et al. (2016), (3) Esplin et al. (2016), (4) Cushing et al. (2016), (5) Leggett et al. (2016).

Table 6
Best-fit Parameters for Equation (1)

	J-band	*Spitzer* [3.6 μm]
A_0	14.69 ± 0.11	3.20 ± 0.06
κdx	6.85 ± 0.07	0.56 ± 0.03

Note. Best-fit functions for both bands are plotted in Figure 5.

amplitudes in the mid-IR case are detected in the late Ts and early Ys, in contrast to the *J* band, where high amplitudes are detected in L/T transition objects. Again, the young L-type objects may have slightly enhanced amplitudes when compared to field L-type brown dwarfs (Metchev et al. 2015).

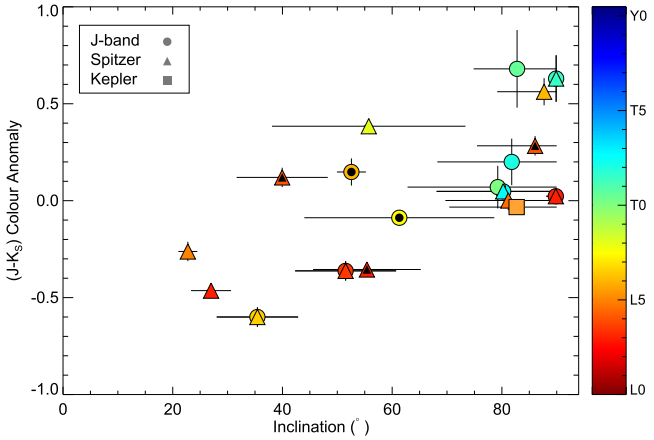

Figure 9. Color anomaly plotted against inclination for the sample in Table 1. Young objects are denoted by a black inset.

5.3. Investigating Color Anomalies of the Sample

We define the color anomaly of each object as the median 2MASS $J - K_S$ color subtracted from the $J - K_S$ color of the object. Median colors for L0–T6 objects were taken from Schmidt et al. (2010). For 2M0050, the T7 object, we calculated the median of all IR T7 objects from DwarfArchives.org (20 objects) and found the median T7 $J - K_S$ color to be -0.04 ± 0.43. This is a much higher error than those in Schmidt et al. (2010) and was thus left out of the analysis. With no $J - K_S$ measurement of Y dwarfs, it was not possible to include WISE0855, WISE1405, and WISE1738. Liu et al. (2016) provides linear relations between spectral type and absolute magnitude for VL-G and INT-G brown dwarfs, and these were used to calculate the median colors for the low-gravity sample.

Figure 9 displays the color anomaly of objects listed in Table 1 plotted against their inclinations. We note a correlation between the $J - K_S$ color anomaly and inclination, whereby objects viewed equator-on appear redder than objects viewed at lower inclinations.

Calculating the correlation coefficient and *p*-value, we find that the relation between color anomaly and inclination is statistically significant with a *p*-value = 0.4%. Objects we observe to be redder than the median are viewed equator-on, whereas objects appearing bluer than the median are viewed closer to pole-on. This result could be interpreted by the idea first proposed by Kirkpatrick et al. (2010), that the viewing angle determines the spectral appearance of a brown dwarf. This could occur when clouds are not homogenously distributed in latitude or when grain size and cloud thickness vary in latitude. Our results can be explained if thicker or large-grained clouds are situated at the equator, while thinner or small-grained clouds are situated at the poles.

Figures 10 and 11 show the variability amplitude plotted against the color anomaly for *J*-band and *Spitzer* detections, respectively. Both plots exhibit a consistent trend, whereby field objects that are redder than the median display higher *J*-band and *Spitzer* variability amplitudes. The field objects with the highest observed variability amplitudes are those with the reddest $J - K_S$ colors of their spectral type. We find that this correlation is significant at the 93% and 99% levels for the *J*-band and mid-IR detections, respectively. This relation may

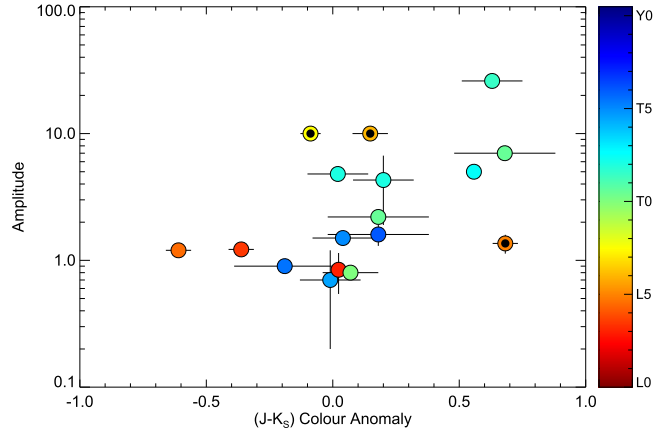

Figure 10. Amplitude plotted against color anomaly for *J*-band variability detections.

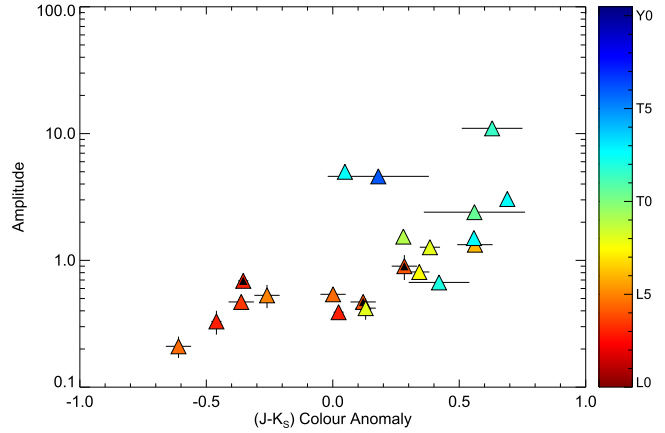

Figure 11. Amplitude plotted against color anomaly for *Spitzer* variability detections.

be explained by consideration of viewing angle. If redder brown dwarfs are viewed equator-on, and equator-on objects exhibit the highest amplitudes, then it follows that redder brown dwarfs should display the highest variability amplitudes. Similarly, bluer brown dwarfs are viewed close to pole-on, so the observed variability amplitude will be reduced because of the viewing angle.

We also see trends related to spectral type in both figures that could explain the observed relation. In the *J*-band case (Figure 10), the early- to mid-L spectral type field dwarfs display a blue anomaly, while the L/T transition field dwarfs display a red ($J - K_S$) color anomaly. The late-T type objects with detected variability display colors that are relatively close to the median. These trends are shown even more clearly for the *Spitzer* detections (Figure 11). The low-amplitude variability detections are observed in early-L type brown dwarfs displaying a blue anomaly. We observe higher amplitude variability in L/T transition objects that display a red anomaly. This trend could be explained by variability that is due to the breakup of silicate clouds. L-type brown dwarfs with thick silicate clouds generally appear red, while the relatively cloudless T dwarfs appear more blue. Thus, L dwarfs whose clouds have begun to break up will appear bluer than the median, and produce variability that is due to these patchy clouds. On the other hand, early-T dwarfs that still have clouds in their atmospheres will appear redder than the median, resulting in photometric variability as these clouds rotate in and out of view. While this simple idea is an attractive explanation, spectroscopic variability observations have shown that cloud evolution in L and T brown dwarf atmospheres is significantly more complex than simple formation of cloud holes (Buenzli et al. 2012, 2015b; Apai et al. 2013; Yang et al. 2016).

Furthermore, we see that surface gravity has an effect on this relation in both bands. For the *J*-band detections (Figure 10), the low-surface gravity objects do not seem to follow the trend in spectral type, and appear among the L/T transition field objects. It seems that low-surface gravity objects that are redder than the median appear variable, but with only three detections we cannot confirm this. In contrast, for the *Spitzer* detections, two-thirds of the low-surface gravity objects seem to follow the overall trend, with one object falling closer to the L/T transition field brown dwarfs. Variability surveys of young, low-surface gravity objects will clarify these possible deviations from the field brown dwarf population.

6. Summary and Conclusions

In this paper we explored the effects of inclination angle on measured variability amplitudes and whether brown dwarfs display similar intrinsic amplitudes. We furthermore proceeded to examine the relation between inclination angle and spectral appearance. We determined the inclination angle of 19 variable brown dwarfs using archival Keck data and estimates on radius. We analyzed the full sample of L, T, and Y spectral type brown dwarfs with published *J*-band and *Spitzer* variability detections.

We conclude that brown dwarfs have different intrinsic amplitudes, dependent on properties such as spectral type, rotation period, and surface gravity. In this paper we find evidence that the variability amplitude may increase with rotational period for periods $<$7–9 hr. This result is significant at the 93% level for *J*-band detections, but is not significant for *Spitzer* detections. The inclination angle affects the observed amplitude through a projection effect as well as atmospheric attenuation. Our toy model suggests that *J*-band variability is more strongly affected by inclination than *Spitzer* variability. The reason may be that the *J*-band probes deeper levels in the atmosphere. The result is that the flux coming from these deeper levels is more attenuated because the path lengths increase at lower inclinations. All brown dwarfs with mid-IR variability detections are inclined at an angle $>20°$. In the near-IR, we find that all brown dwarfs with *J*-band variability detections are inclined at an angle $>35°$.

We find a trend between the color anomaly and inclination of our sample that is statistically significant at the 99% level. Field objects viewed equator-on appear redder than the median for their spectral type, whereas objects viewed at lower inclinations appear bluer. This supports the idea that our viewing angle influences the spectral and photometric appearance of a brown dwarf. These results can be explained if thicker or large-grained clouds are situated at the equator, with thinner or small-grained clouds at the poles. We also find a strong correlation between color anomaly and both mid-IR and *J*-band variability, where redder objects have higher variability amplitudes. This again suggests that the spectral appearance of a brown dwarf is strongly affected by its inclination angle.

The authors would like to thank Jack Gallimore for his contributions to the fitting code. J.M.V. acknowledges the support of the University of Edinburgh via the Principal's Career Development Scholarship. K.N.A. acknowledges

support from the Isaac J. Tressler Fund for Astronomy at Bucknell University. B.B. gratefully acknowledges support from STFC grant ST/M001229/1.

References

Allard, F., Homeier, D., & Freytag, B. 2012, RSPTA, 370, 2765
Allers, K. N., Gallimore, J. F., Liu, M. C., & Dupuy, T. J. 2016, ApJ, 819, 133
Allers, K. N., & Liu, M. C. 2013, ApJ, 772, 79
Apai, D., Radigan, J., Buenzli, E., et al. 2013, ApJ, 768, 121
Artigau, É, Bouchard, S., Doyon, R., & Lafrenière, D. 2009, ApJ, 701, 1534
Bailer-Jones, C. A. L. 2004, A&A, 419, 703
Basri, G., Mohanty, S., Allard, F., et al. 2000, ApJ, 538, 363
Berger, E., Rutledge, R. E., Reid, I. N., et al. 2005, ApJ, 627, 960
Bertoldi, F., Timmermann, R., Rosenthal, D., Drapatz, S., & Wright, C. M. 1999, A&A, 346, 267
Biller, B. A., Crossfield, I. J. M., Mancini, L., et al. 2013, ApJL, 778, L10
Biller, B. A., Vos, J., Bonavita, M., et al. 2015, ApJL, 813, L23
Blake, C. H., Charbonneau, D., & White, R. J. 2010, ApJ, 723, 684
Buenzli, E., Apai, D., Morley, C. V., et al. 2012, ApJL, 760, L31
Buenzli, E., Apai, D., Radigan, J., Reid, I. N., & Flateau, D. 2014, ApJ, 782, 77
Buenzli, E., Marley, M. S., Apai, D., et al. 2015a, ApJ, 812, 163
Buenzli, E., Saumon, D., Marley, M. S., et al. 2015b, ApJ, 798, 127
Burrows, A., Hubbard, W. B., Lunine, J. I., & Liebert, J. 2001, RvMP, 73, 719
Clarke, F. J., Hodgkin, S. T., Oppenheimer, B. R., Robertson, J., & Haubois, X. 2008, MNRAS, 386, 2009
Croll, B., Muirhead, P. S., Han, E., et al. 2016, arXiv:1609.03586
Crossfield, I. J. M., Biller, B., Schlieder, J. E., et al. 2014, Natur, 505, 654
Cruz, K. L., Kirkpatrick, J. D., & Burgasser, A. J. 2009, AJ, 137, 3345
Cushing, M. C., Hardegree-Ullman, K. K., Trucks, J. L., et al. 2016, ApJ, 823, 152
Cushing, M. C., Roellig, T. L., Marley, M. S., et al. 2006, ApJ, 648, 614
Cushing, M. C., Vacca, W. D., & Rayner, J. T. 2004, PASP, 116, 362
Enoch, M. L., Brown, M. E., & Burgasser, A. J. 2003, AJ, 126, 1006
Esplin, T. L., Luhman, K. L., Cushing, M. C., et al. 2016, ApJ, 832, 58
Faherty, J. K., Burgasser, A. J., Walter, F. M., et al. 2012, ApJ, 752, 56
Faherty, J. K., Riedel, A. R., Cruz, K. L., et al. 2016, ApJS, 225, 10
Filippazzo, J. C., Rice, E. L., Faherty, J., et al. 2015, ApJ, 810, 158
Folkes, S. L., Pinfield, D. J., Kendall, T. R., & Jones, H. R. A. 2007, MNRAS, 378, 901
Gagné, J., Faherty, J. K., Burgasser, A. J., et al. 2017, ApJL, 841, L1
Gagné, J., Faherty, J. K., Cruz, K. L., et al. 2015, ApJS, 219, 33
Gillon, M., Triaud, a. H. M. J., Jehin, E., et al. 2013, A&A, 555, L5
Girardin, F., Artigau, É., & Doyon, R. 2013, ApJ, 767, 61
Gizis, J. E., Allers, K. N., Liu, M. C., et al. 2015, ApJ, 799, 203
Gizis, J. E., Burgasser, A. J., Berger, E., et al. 2013, ApJ, 779, 172
Gizis, J. E., Faherty, J. K., Liu, M. C., et al. 2012, AJ, 144, 94
Harding, L. K., Hallinan, G., Boyle, R. P., et al. 2013, ApJ, 779, 101
Heinze, A. N., Metchev, S., & Kellogg, K. 2014, ApJ, 767, 173
Jackson, R. J., & Jeffries, R. D. 2010, MNRAS, 402, 1380
Karalidi, T., Apai, D., Marley, M. S., & Buenzli, E. 2016, ApJ, 825, 90
Kirkpatrick, J. D., Looper, D. L., Burgasser, A. J., et al. 2010, ApJS, 190, 100
Kostov, V., & Apai, D. 2013, ApJ, 762, 47
Leggett, S. K., Cushing, M. C., Hardegree-Ullman, K. K., et al. 2016, ApJ, 830, 141
Lew, B. W. P., Apai, D., Zhou, Y., et al. 2016, ApJL, 829, L32
Liu, M. C., Dupuy, T. J., & Allers, K. N. 2016, ApJ, 833, 96
Liu, M. C., Magnier, E. A., Deacon, N. R., et al. 2013, ApJL, 777, L20
Looper, D. L., Mohanty, S., Bochanski, J. J., et al. 2010, ApJ, 714, 45
Luhman, K. L. 2014, ApJL, 786, L18
Madhusudhan, N., Burrows, A., & Currie, T. 2011, ApJ, 737, 34
Marocco, F., Day-Jones, A. C., Lucas, P. W., et al. 2014, MNRAS, 439, 372
Metchev, S., Apai, D., Radigan, J., et al. 2013, AN, 334, 40
Metchev, S. A., Heinze, A., Apai, D., et al. 2015, ApJ, 799, 154
Press, W. H., Teukolsky, S. A., Vetterling, W. T., & Flannery, B. P. 2007, Numerical Recipes: The Art of Scientific Computing (3rd ed.; New York: Cambridge University Press)
Radigan, J. 2014, ApJ, 797, 120
Radigan, J., Jayawardhana, R., Lafrenière, D., et al. 2012, ApJ, 750, 105
Radigan, J., Lafrenière, D., Jayawardhana, R., & Artigau, E. 2014, ApJ, 793, 75
Reiners, A., & Basri, G. 2008, ApJ, 684, 1390
Rhines, P. 1970, GApFD, 1, 273
Schmidt, S. J., West, A. A., Hawley, S. L., & Pineda, J. S. 2010, AJ, 139, 1808
ter Braak, C., & Vrugt, J. 2008, Statistics and Computing, 18, 435
Walkowicz, L. M., Basri, G., & Valenti, J. a. 2013, ApJS, 205, 17
Wilson, P. A., Rajan, A., & Patience, J. 2014, A&A, 566, A111
Yang, H., Apai, D., Marley, M. S., et al. 2016, ApJ, 826, 8
Zhou, Y., Apai, D., Schneider, G. H., Marley, M. S., & Showman, A. P. 2016, ApJ, 818, 176